Analysis of losses in superconducting magnets based on the Nb$_3$Sn Rutherford cable configuration for future gantries

M Breschi[1] , **L Cavallucci**[1] , **P L Ribani**[1]**, C Calzolaio**[2] **and S Sanfilippo**[2]

[1] DEI, Department of Electrical, Electronic and Information Engineering, University of Bologna, Italy
[2] PSI, Paul Scherrer Institut, Villigen, Switzerland

E-mail: lorenzo.cavallucci3@unibo.it

Abstract

Proton therapy for the treatment of cancers adopts a rotating gantry to irradiate the tumor from any direction. The gantry system consists of different beamline magnets that bend the proton beam towards the patient. The use of superconducting magnets allows reducing the size and weight of the last bending section. During the gantry operation, it is necessary to change the magnetic field of the last bending section in order to vary the proton penetration depth. This change determines electrodynamic transients in the superconducting strands and cables that generate losses. A thorough computation of these losses is essential for a safe design of the cryogenic system. Two main types of losses must be accounted for when dealing with multistrand superconducting cables, related to the magnetization and coupling of the superconducting filaments (intrastrand losses) and to the current loops induced between different strands during electrodynamic transients (interstrand losses). This work describes the methodologies and numerical codes adopted to compute the hysteresis and coupling losses in an innovative magnet system designed by the Paul Scherrer Institute for future superconducting gantries. In this design the superconducting coils are wound using Nb$_3$Sn Rutherford cables. The validation of the numerical tools versus analytical results is presented for simplified cases with uniform magnetic flux density applied to the conductor. The results of the losses calculation and the impact of the different contributions are then presented for the actual proposed magnet system configuration.

Keywords: superconducting magnets, AC losses, Nb$_3$Sn, Rutherford cable, gantry magnet

(Some figures may appear in colour only in the online journal)

1. Introduction

Medical therapies based on ion or proton beams are widely developing for cancer treatment due to their capability to irradiate the tumor from different directions in order to reduce the dose on the normal cells. The radiation dose delivered to the target volume is maximized and the dose to the surrounding normal tissues is minimized [1–3]. Many facilities use rotatable gantry beamlines to direct the proton or ion beam to the patient from different angles [4].

The proton or ion therapy facilities are composed of beamline magnets, beam diagnostic elements and the mechanical support structure. The gantry magnet system is the final section of these facilities; it rotates around the patient and allows irradiating the tumor from different directions. These systems can be extremely heavy and cumbersome: as an example, the gantry magnet system of the Heidelberg Carbon Ion Gantry facility weighs 600 tons [4], and the Proton Therapy Gantry 2 of the Paul Scherrer Institute (PSI) weighs 200 tons [5]. A remarkable step forward in the direction of designing more compact and lighter gantries could be achieved by means of superconducting magnets, in particular for the final bending sectionthat has a large aperture. The high field intensities that can be achieved with superconducting magnets allow decreasing the bending radius and, therefore, the overall weight and footprint of the system,

with consequent reduction of the total size and complexity of the mechanical structure. Moreover, superconducting magnets allow reaching higher magnetic field gradients, which allows increasing the momentum acceptance of the particle beam. This feature reduces the need to ramp the magnet, which allows covering a large momentum spread, and enables new treatment techniques [6, 7].

Recently, superconducting magnets have been designed and built for the carbon ion gantry at the National Institute of Radiological Sciences in Chiba (Japan) and for a proton gantry developed by the US company Pro-Nova [8–10]. These first superconducting gantry systems are currently under commissioning [11]. An R&D project to reduce the size of rotating gantry systems is presently in progress at the PSI [1, 2], Switzerland, with the aim of developing a superconducting magnet system wound with Nb$_3$Sn Rutherford cables. The use of coolant for the magnet mounted on a rotating gantry is extremely difficult, and therefore, a conduction cooling option has been selected for this project. As already mentioned, the magnetic field of the rotating gantry has to vary in time depending on the energy of the particle beam. These electrodynamic transients generate losses in the superconducting coils, both due to hysteresis and to coupling currents. Moreover, some particles escaping from the nominal trajectory (beam losses), may collide with the coils causing thermal inputs that can result in a poor thermal stability of the conduction cooled coils. Therefore, the determination of coupling and hysteresis ac losses in relation with the magnetic field cycle is essential to ensure the thermal stability of a gantry magnet [12].

The state of the art for superconducting gantry systems is based on NbTi magnets. The analysis of losses and stability on NbTi gantry magnets is relatively widely analyzed in literature. Experimental tests of thermal stability on NbTi gantry magnets are presented in [12], whereas theoretical analyses are described in [13] and [14]. Superconducting materials other than NbTi, such as Nb$_3$Sn and HTS have several advantages due to their increased current carrying capability and temperature margin, but have been usually ruled out due to cost and difficulties associated with magnet fabrication (such as conductor heat treatments on the winding tapes). Detailed studies of available temperature margins have to be carried out to determine the capabilities of Nb$_3$Sn and HTS materials for their application in gantry systems [14]. A few studies have been presented to determine the advantages and overall thermal stability of HTS materials for gantry magnet systems [15, 16]. Meanwhile, the temperature margin and ac losses for Nb$_3$Sn gantry magnets have not been thoroughly analyzed yet.

In this work, a detailed numerical analysis is presented for the determination of temperature increase related to coupling and hysteresis losses during the working scenario of the Nb$_3$Sn gantry magnet under development at the PSI [1, 2]. The THELMA code developed at the University of Bologna, validated for the study of cable in conduit conductors for the ITER project [17, 18], is adapted here to the analysis of ac losses in the Nb$_3$Sn Rutherford cable configuration. The model of the Rutherford cable is based on a distributed parameter circuit approach, that was proved suitable for the analysis of long range coupling currents both with numerical
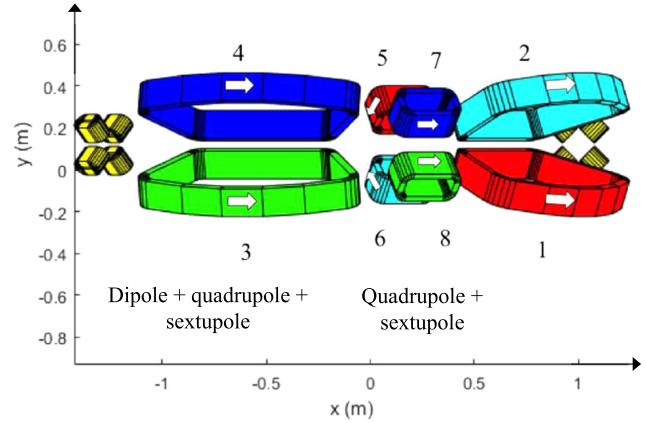

Figure 1. Layout of the gantry magnetic system as implemented in the THELMA code model. The split of the curvilinear part of each coil in five segments is only made for graphical representation purposes.

[19, 20] and analytical studies [21–23]. The main development of the model adopted in this work with respect to the models presented in [19–23] consists in the adoption of non-homogenous interstrand contact conductances along the cable length, which allow a proper description of the short range coupling currents and related losses. The computation of coupling losses is validated in simplified cases versus analytical formulae available in the literature. Then, the coupling and hysteresis losses during the gantry magnet system operating transport current cycle are computed with THELMA, and implemented in a thermal model developed in the COMSOL Multiphysics environment [24]. Finally, the computed temperature distribution of the coils is compared with the current sharing temperature to determine the temperature margin during the operating current cycle.

2. Gantry magnet system configuration

The magnetic flux density in accelerator magnets is usually represented through a series development, in which the various components are referred to as field harmonics [25]:

$$B_y + jB_x = \sum_{n=1}^{\infty} (B_n + jA_n)\left(\frac{x + jy}{r_0}\right)^{n-1}, \qquad (1)$$

where r_0 is a reference radius, B_n is the normal $2n$-pole component of the magnetic field and A_n is the skew $2n$-pole component of the magnetic field.

In a former study a configuration of superconducting gantry magnet system proposed by PSI was presented in [1]. Several modifications to improve the magnetic system were then implemented in the configuration presented in [2], which is the one analyzed in the present study. In this configuration, the dipolar field used to bend the protons to the patient location is produced by racetrack coils. The combined function magnet system configuration includes 8 main coils and two end quadrupoles, as shown in figure 1.

The main dipole field component is provided by coils #1, #2, #3, #4. These coils also contribute with two other

Table 1. Main geometric data of the coils.

Coils N. 1, 2, 3, 4

Cross section Width	40 mm
Cross section Height	140 mm
Number of layers (in the width direction)	27
Number of turns per layer (in the height direction)	28
Total number of turns	756
Cross section of cable with insulation in the coil	7.41 mm^2 (1.48 mm × 5.00 mm)
Length of the coil axis	2.65 m

Coils N. 5, 6, 7, 8

Cross section Width	31 mm
Cross section Height	150 mm
Number of layers (in the width direction)	21
Number of turns per layer (in the height direction)	30
Total number of turns	630
Cross section of cable with insulation in the coil	7.38 mm^2 (1.48 mm × 5.00 mm)
Length of the coil axis	0.794 m

Coils N. 9, 10, 11, 12, 13, 14, 15, 16

Cross section Width	40 mm
Cross section Height	100 mm
Length of the coil axis	0.215 m

Table 2. Main data of the rutherford cable.

Type of cable	Rutherford
Twist Pitch	70 mm
Number of strands	12
Strand diameter	0.82 mm
lay angle	8.0 deg
Keystone angle	0 deg
Cu:nonCU	0.93
RRR	100
Width	4.9 mm
Thickness	1.45 mm
Critical current (4.2 K, 8 T, −22%)	363 A

Table 3. Main data of the composite superconducting wire.

Material	Area	% fraction
Cu	3.05 10^{-6} m^2	41.2
Nb$_3$Sn	1.64 10^{-6} m^2	22.2
Epoxy	1.07 10^{-6} m^2	14.5
Bronze	1.64 10^{-6} m^2	22.2
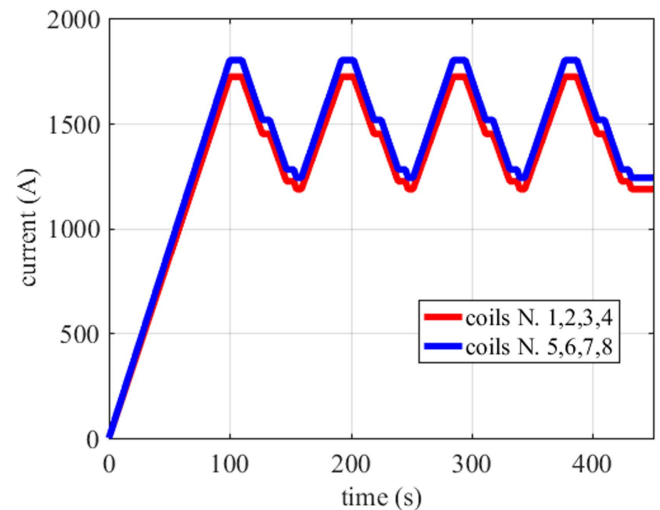
Figure 2. Evolution in time of the transport currents of the eight main coils of the PSI gantry magnet system during a typical operating cycle.

harmonics, namely a quadrupole and a sextupole field component. The coils #5, #6, #7, and #8, located in the middle of the magnet configuration, mainly contribute to the magnetic flux density with a quadrupole and a sextupole component. The end quadrupoles (with indices from #9 to #16) provide essentially a quadrupole component and consist of four copper racetrack coils. The magnetic geometry is such to produce a FODO structure (the term 'FODO' describes a sequence of focusing, F, and defocusing, D, quadrupole magnets with dipole magnets or drift spaces denoted by 'O') with the first quadrupole focusing in the bending plane. The superposition of dipole and quadrupole fields allows having locally achromatic bending sections without increasing the gantry size. For this reason it is important to use combined function magnets [6]. In optics rays of different wavelength find a different refraction index in a lens and therefore they experience a different focal length producing chromatic aberrations. In analogy to that, particles of different momentum see a different focusing strength in the quadrupoles. To correct the natural chromaticity produced by the focusing elements, a sextupole field component is added. In a sextupole a particle passing off-center receives a kick proportional to the square of its displacement from the center. A sextupole acts then as a quadrupole with a focusing strength proportional to the displacement from the center.

The main geometric data concerning the magnet system design are reported in table 1. In the present configuration, the same Nb$_3$Sn Rutherford cable structure is adopted for winding all the coils (#1–#8). The cable is not keystoned and

composed of 12 Nb$_3$Sn strands. The main data of the Rutherford cable are reported in table 2, whereas the main data concerning the superconducting wire are reported in table 3. The parameterization of the critical surface of the wire adopting the ITER—like parameterization is reported in [26].

The reference working scenario of the gantry magnet system is characterized by a series of transport current ramps and plateaus as shown in figure 2. The transport currents in the coils from #1 to #4 are identical, since they are connected in series; the same holds for the transport currents in the coils from #5 to #8. All transport currents exhibit an initial ramp to their maximal value, followed by several cycles between this maximum and an intermediate current level set to 2/3 of the maximal current level. The transport current scenario is based on a worst case treatment scenario

where four fields are applied each having a large depth extension requiring three magnets ramps per layer.

3. Model Description and loss computation methodologies

3.1. Model description

The electromagnetic model of the Rutherford cable in THELMA code [17, 18] is based on a distributed parameter circuit approach. The equations of the model are derived from the Magneto-Quasi-Static formulation of the Maxwell equations. In order to discretize the Rutherford cable geometry, a single strand is a cable element (CE) of the model and the number of cable elements (NCE) of the model coincide with the number of strands. The unknowns of the problem are the values of the difference currents (i_α with $\alpha = 1, …, NCE$) of the CEs with respect to a uniform current distribution.

$$i_\alpha = I_\alpha - \frac{I}{NCE} \quad \text{with } \alpha = 1, …, NCE, \quad (2)$$

where I_α is the current in the αth CE and I is the total current of the cable.

The scalar electrical potential and the magnetic vector potential are solved. The current density continuity condition is added to compute the current density in each CE.

$$\mathbf{E}(\mathbf{P}, t) = -\Delta V - \frac{\partial}{\partial t} \left[\frac{\mu_0}{4\pi} \int_\Omega \frac{\mathbf{J}(\mathbf{Q}, t)}{|\mathbf{P} - \mathbf{Q}|} \mathrm{d}^3\mathbf{Q} \right], \quad (3)$$

$$\nabla \cdot \mathbf{J} = 0. \quad (4)$$

The closure of equations is obtained by the power law as a constitutive law of the superconducting material. The other materials that compose the strand are supposed in parallel with the superconducting one.

The self and mutual per unit length induction coefficients are numerically calculated from geometrical parameters of the cable (twist pitches, cable-axes trajectory, strand diameter etc). From the geometrical parameters is also computed the per-unit-length conductance between CEs as a function of the longitudinal coordinate.

3.2. Hysteresis losses

The electrodynamic losses are generated mainly during the current ramps and are due to both the hysteresis and coupling losses. The equations of the electrodynamic model implemented in the THELMA code [17, 18] allow one to compute the current distribution between the strands and the corresponding coupling losses. The current sharing between strands occurs through either a uniform or a variable contact conductance per unit length. In both cases, the per unit length conductances are computed in order to obtain given values of the adjacent (R_a) and crossover (R_c) resistances [27] respectively set to 50 and 100 $\mu\Omega$.

The determination of the hysteresis losses starts from the calculation of the effective diameter (d_{eff}) of the strand. In the present analysis, the Nb$_3$Sn strand selected for the magnet system design owes to the pool of the ITER strands. The d_{eff} is computed from the magnetization cycle obtained experimentally, and is equal to 7.8 μm for this wire.

The local value of the power dissipated per unit volume due to the hysteresis losses is then given by the following expression [28]

$$P\left[\frac{W}{m^3}\right] = \frac{2}{3\pi}\mu_0 J_c(B, T, \varepsilon)\lambda d_{eff} \left| \frac{\mathrm{d}B}{\mathrm{d}t} \right|, \quad (5)$$

where J_c is the critical current density as a function of the temperature T, magnetic flux density B and strain ε; λ is the superconductor fraction; d_{eff} is the effective diameter of the strand and $\left| \frac{\mathrm{d}B}{\mathrm{d}t} \right|$ is the time derivative of the magnetic flux density.

This formula requires the knowledge of the field distribution at every coil location: from this input both the local value of the critical current density and of the time derivative of the magnetic flux density can be computed.

3.3. Coupling losses

The validation of the THELMA model [17, 18] for the calculation of the coupling losses was carried out in a simplified test case, by comparison with two analytical formulae available in the literature [29, 30]. The selected case study consists of a rectilinear Rutherford cable composed by 14 strands, without transport current, subjected to a uniform magnetic field applied orthogonally to the broad face of the cable. The time dependence of the magnetic field follows a triangular wave from 0 to 3 T, with a variable ramp rate.

The comparison between the analytical and the numerical THELMA results are performed with two different models. In a first approximate model the per unit length conductance is assumed uniform along the cable length; the value selected is equivalent to the overall resistance between the two strands over one cable twist pitch given by the local contact resistances between two strands. A second approach is based on the definition of a variable contact conductance between the strands. The variable conductance is calculated from the geometrical model assuming a given value of the per unit surface conductance, which is implemented as a fitting parameter.

A convergence study was performed by changing the number of mesh elements per twist pitch in the numerical simulations. The comparison between the numerical and analytical results is presented in table 4. The results clearly indicate that the model based on a uniform contact conductance per unit length, which is suitable for the calculation of long range coupling currents [19], is not suited for the analysis of short range coupling currents, as it underestimates the losses due to coupling currents. The results show that the model with non-uniform contact conductances between strands is suitable to compute the losses due to coupling currents; the number of mesh elements in a twist pitch does not significantly affect the results. In the case of 14 mesh elements per twist pitch, only one mesh point is included in every crossover contact between non-adjacent strands. In the 28 and 42 mesh element cases, each contact is discretized

Table 4. Thelma model results with $\dot{B} = 1$ T S^{-1}.

Number of elements in a twist pitch	Q (mW m^{-1}) constant conductance model	Q (mW m^{-1}) variable conductance model	Q (mW m^{-1}) Sytnikov [29]	Q (mW m^{-1}) Akhmesov [30]
	magnetic flux density field perpendicular to the large surface of the cable			
14	21.45	35.07	36.38	35.86
28	21.31	34.55		
42	21.30	35.86		

Table 5. Thelma versus analytical results.

$\dot{B}$ (T s^{-1})	Q (mW m^{-1}) variable conductance model	Q (mW m^{-1}) Sytnikov
0.1	0.35	0.36
0.2	1.38	1.46
0.4	5.53	5.82
0.8	22.11	23.28
1.0	35.87	36.38

with two and three mesh point respectively. The convergence study shows that using 28 elements along one cable twist pitch is sufficient for a correct computation of the coupling losses without excessively increasing the computational efforts. This level of mesh refinement was therefore selected for the following analyses. In order to compare analytical and numerical results over a broader range of model parameters, the power loss was computed with variable ramp-rates of the magnetic flux density applied perpendicular to the broad face of the cable. Figure 3 shows the quadratic dependence of the losses on the ramp rate, and a good agreement of numerical and analytical results over the whole range of this parameter is obtained (see table 5), which therefore gives confidence in the modeling approach adopted.

4. Computation of total losses in the gantry magnet system

4.1. Computation of total losses at selected turns of the gantry magnets

The power losses during the electrodynamic transients of the gantry system were computed selecting for each coil a given number of reference turns. In particular, six representative turns for each coil were modeled at the strand level by the THELMA code. The locations of these turns, numbered from #1 to #6, are shown in figure 4. The indication of the trajectory of the Rutherford cable along turn #1 of coil #1 is shown in figure 4(a).

The geometry of the reference turns is reproduced for all the main coils of the gantry magnet system. The total power losses, including hysteresis and coupling losses, are computed by the THELMA code at the representative turns during the typical operating current cycle (see figure 2). As a first step, in order to understand the symmetries of the magnet system, only turns #1, #2, #3 and #4 are considered in the analysis. The total power, integrated over the whole length of each
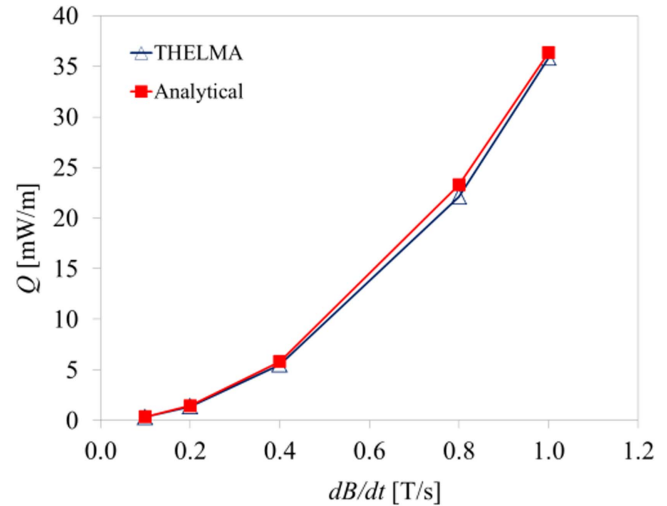
Figure 3. Power per unit length dissipated in the Rutherford cable subjected to a uniform magnetic field applied perpendicular to the cable wide face: numerical versus analytical results.

turn, is divided by the total volume of the turn, including both the cable and the epoxy resin insulation located around each turn, in order to obtain the losses per unit volume.

The total losses per unit volume computed for the coils #1, #2, #3, and #4 are reported in figure 5. It is worth noting that the power evolution follows the operation current profile, with null power losses during the plateau, and a cyclic behavior during the transport current cycles mentioned above. It can be noticed that the computed power loss curves for the coils #1 and #3 are identical; this identity is confirmed for all the representative turns at every location of the coil. The same comment applies for the losses in coils #2 and #4. These identities are related to the symmetry of the gantry magnet system in the present configuration. Moreover the losses in coil #1 and coil #2 are identical once the representative turn #2 is exchanged with turn #4 and turn #1 is exchanged with turn #3. The same consideration holds for the losses in coil #3 and coil #4. These identities derive from simple symmetry considerations about the configuration of the gantry magnet system and of the representative turns geometry shown in figure 4. These arguments lead to the conclusion that all coils #1 through #4 will be characterized by the same temperature distribution at the end of the transport current cycle in adiabatic conditions. Thus, only one coil out of the first four of the gantry magnet system is analyzed for the detailed calculations of the temperature distribution. The selected representative coil for these computations is coil #1.
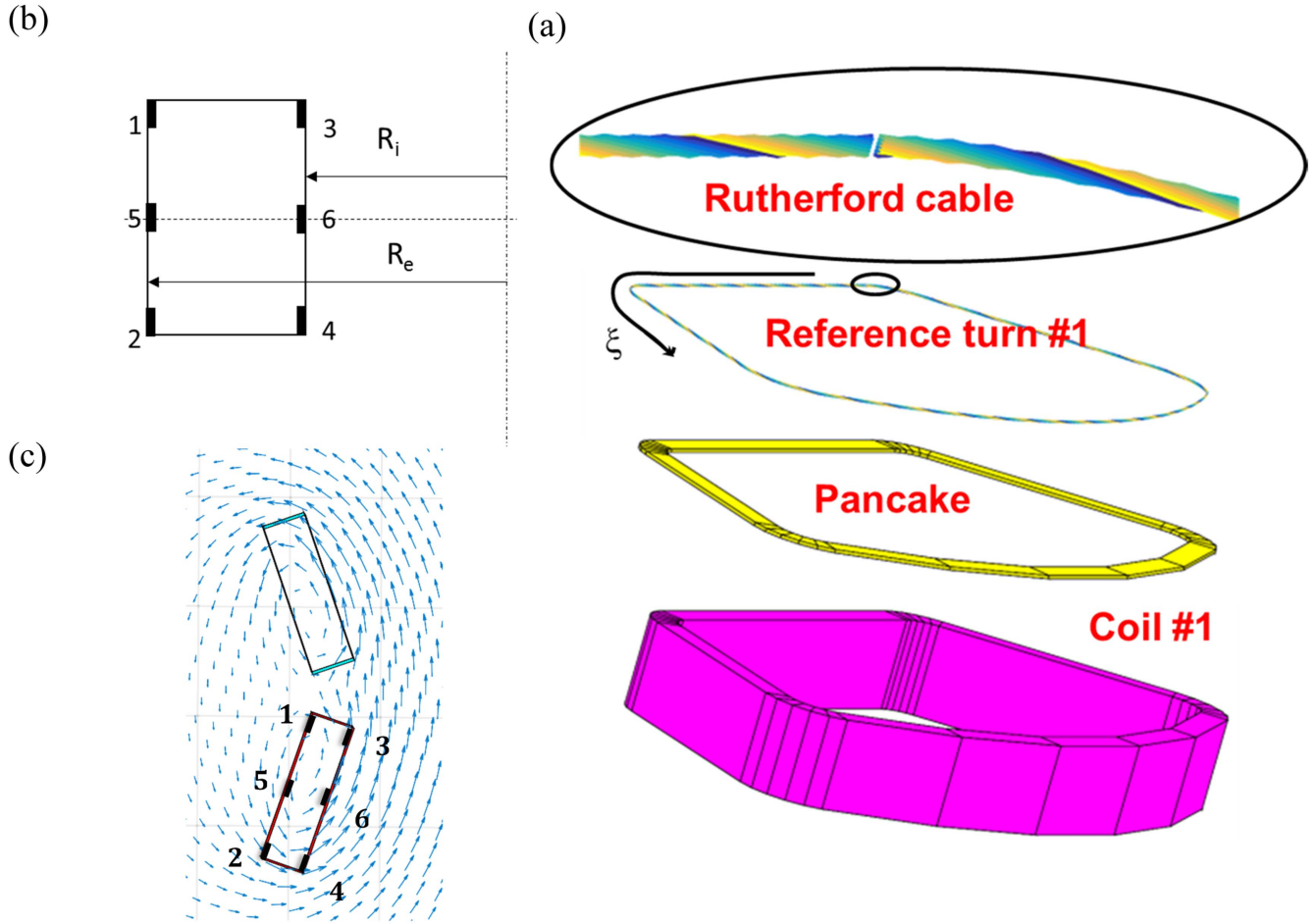
Figure 4. (a) Components of coil #1 used, with indication of the trajectory of the Rutherford cable along turn #1 of coil #1. (b) Position of the representative turns of a coil (figure not to scale). (c) Magnetic flux density lines at the positions of coils #1 and #2 in 2D plot of the coil cross section in the middle plane orthogonal to the *z* axis.

Similar considerations hold for the coils #5, #6, #7, and #8. Therefore, the expected temperature distribution after the transport current cycle in these four coils is practically the same. Thus, only one coil is selected for the temperature distribution computation at representative, namely coil #5.

Once identified the two coils #1 and #5 of interest for the present analysis, a more detailed description of these two is then performed computing the losses in the two additional turns #5 and #6 shown in figure 4(b). The losses at all six representative turns of the coils #1 and #5 are presented in figure 6.

4.2. Results

The flux lines of the magnetic flux density at the locations of coils #1 and #2 are shown in figure 4(c). The modulus of the magnetic flux density is greater at the turns #3, #4 and #6 than at the locations of turns #1, #2 and #5.

In order to understand the dependence of the current distribution on the magnetic flux density inside the coil, the longitudinal variation of the magnetic flux density along selected strands is analyzed here. Figure 7 shows the modulus

of the magnetic flux density field along the cable coordinate for the 6 reference turns of coil #1. The magnetic flux density is highest at turn #6 since it is located close to the magnet bore. The magnetic field exhibits a periodicity with period equal to the twist pitch of the cable, due to the zig-zag path of each strand along the cable length. The magnetic flux density is higher at the internal turns (#1, #2 and #5) then at the external turns (#3, #4 and #6). Therefore, the magnetic flux density differently affects the different turns and the different points A, B, C, D (see figure 8(c)) along the turns. The different power loss regions are related to the impact of the magnetic flux density at the various coil locations. The power loss density along the turns of coil #1 at *t* = 90 s is shown in figure 7(b). It can be noticed that the power loss density along the reference turns is more homogeneous than the magnetic flux density at the turns themselves. The result is due to dominant contribution of the hysteresis losses on the total losses. Moreover, the hysteresis losses depend on the product of the critical current density, which decreases with the magnetic flux density, and the time derivative of the magnetic flux density, which is greater at the high field locations.
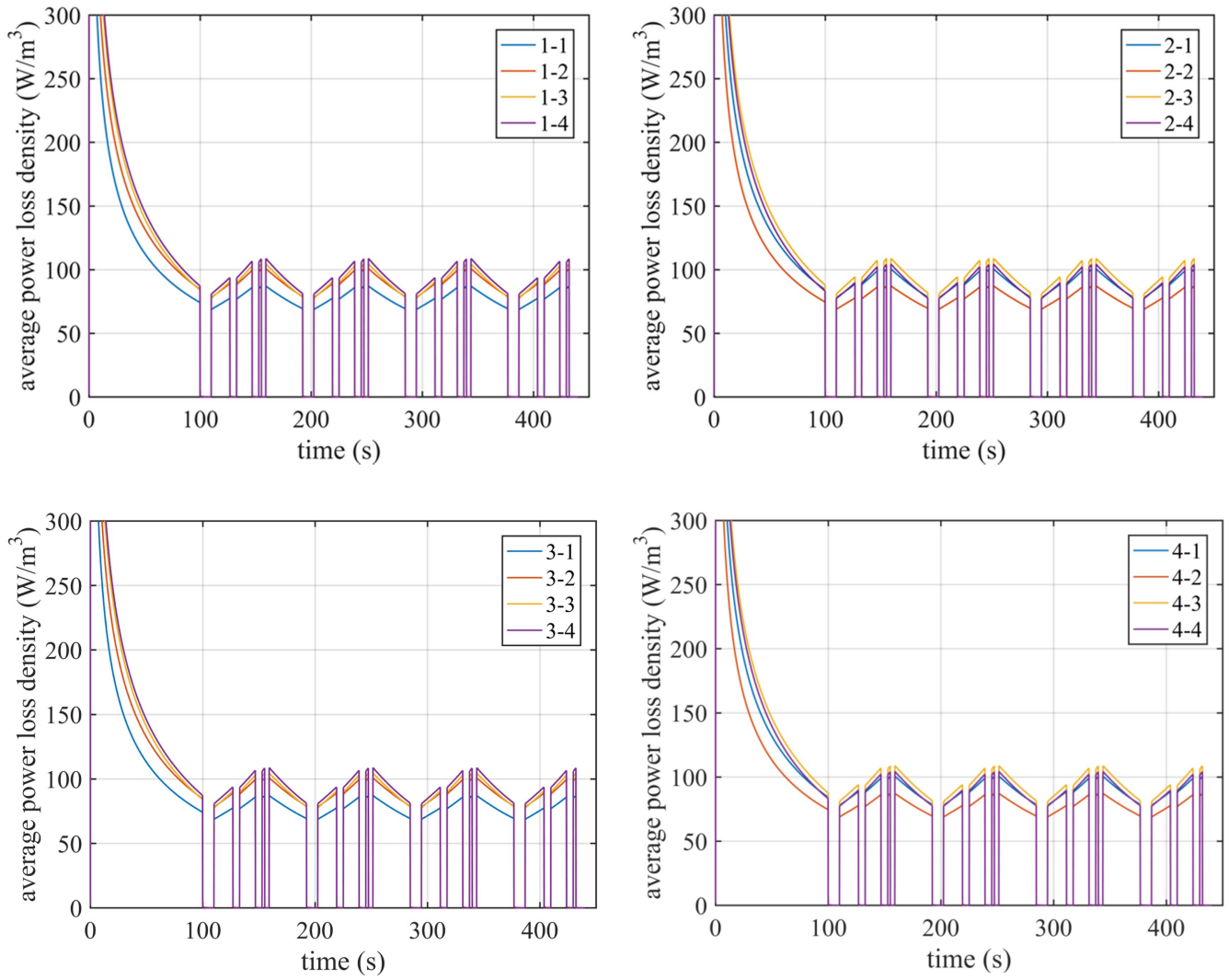
Figure 5. Average power loss per unit volume for the four representative turns of respectively coil #1, coil #2, coil #3, coil #4 computed with uniform current boundary conditions.
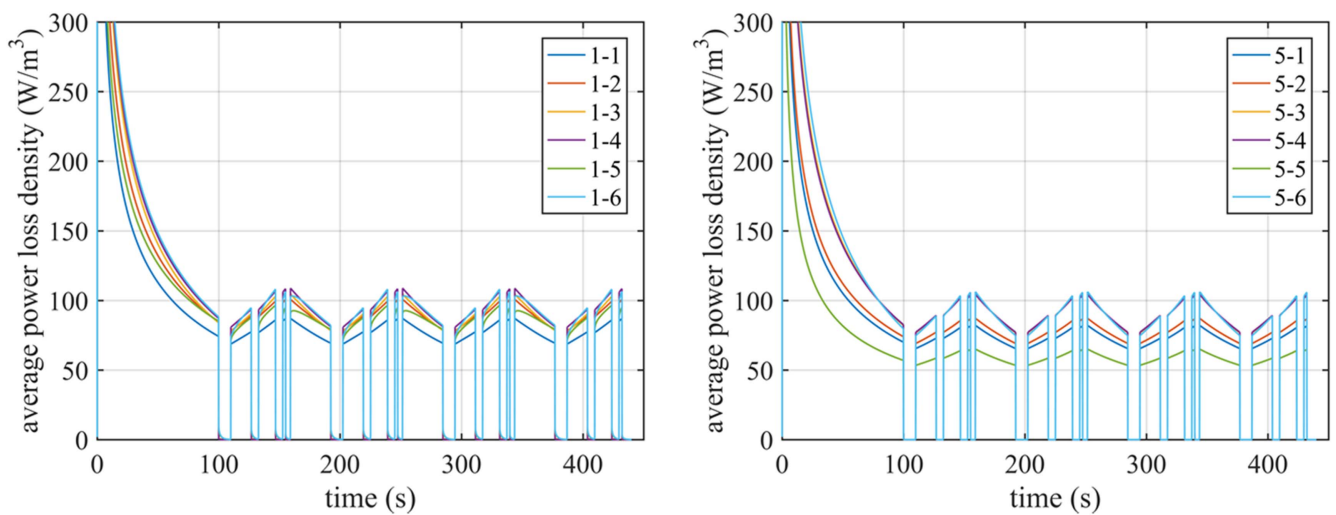

Figure 6. Average power loss per unit volume for the six representative turns of coil #1 and coil #5, computed with uniform current boundary conditions.
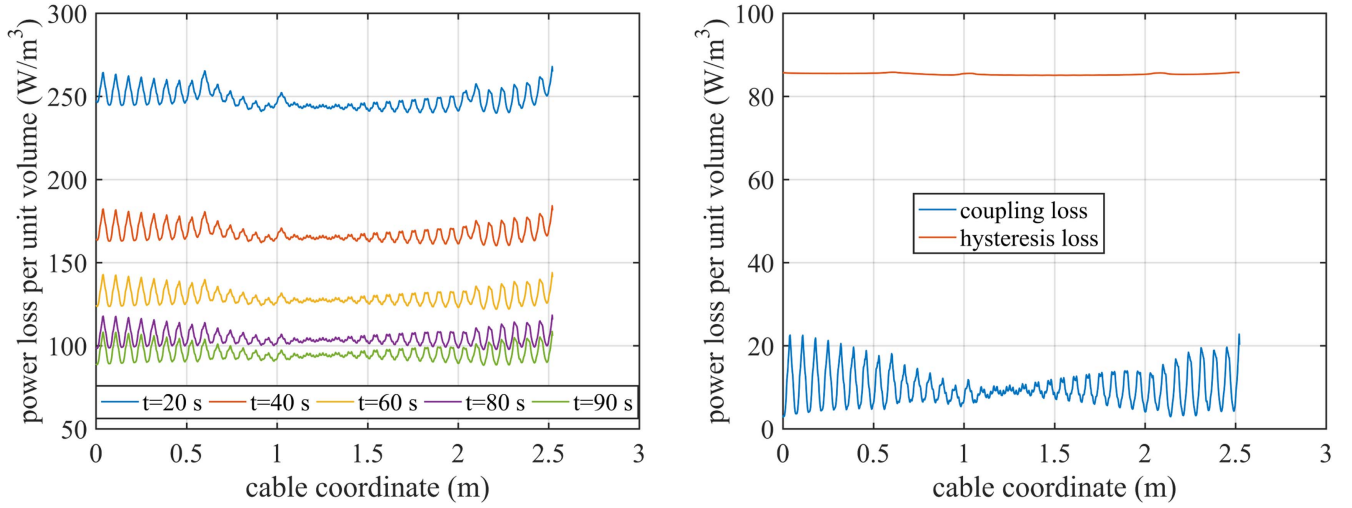
Figure 7. Simulations with uniform current boundary conditions: (a) total power loss along the length (cable coordinate) of turn #4 of coil #1 at $t = 20$ s, $t = 40$ s, $t = 60$ s, $t = 80$ s, $t = 90$ s and (b) coupling and hysteresis losses at $t = 90$ s.
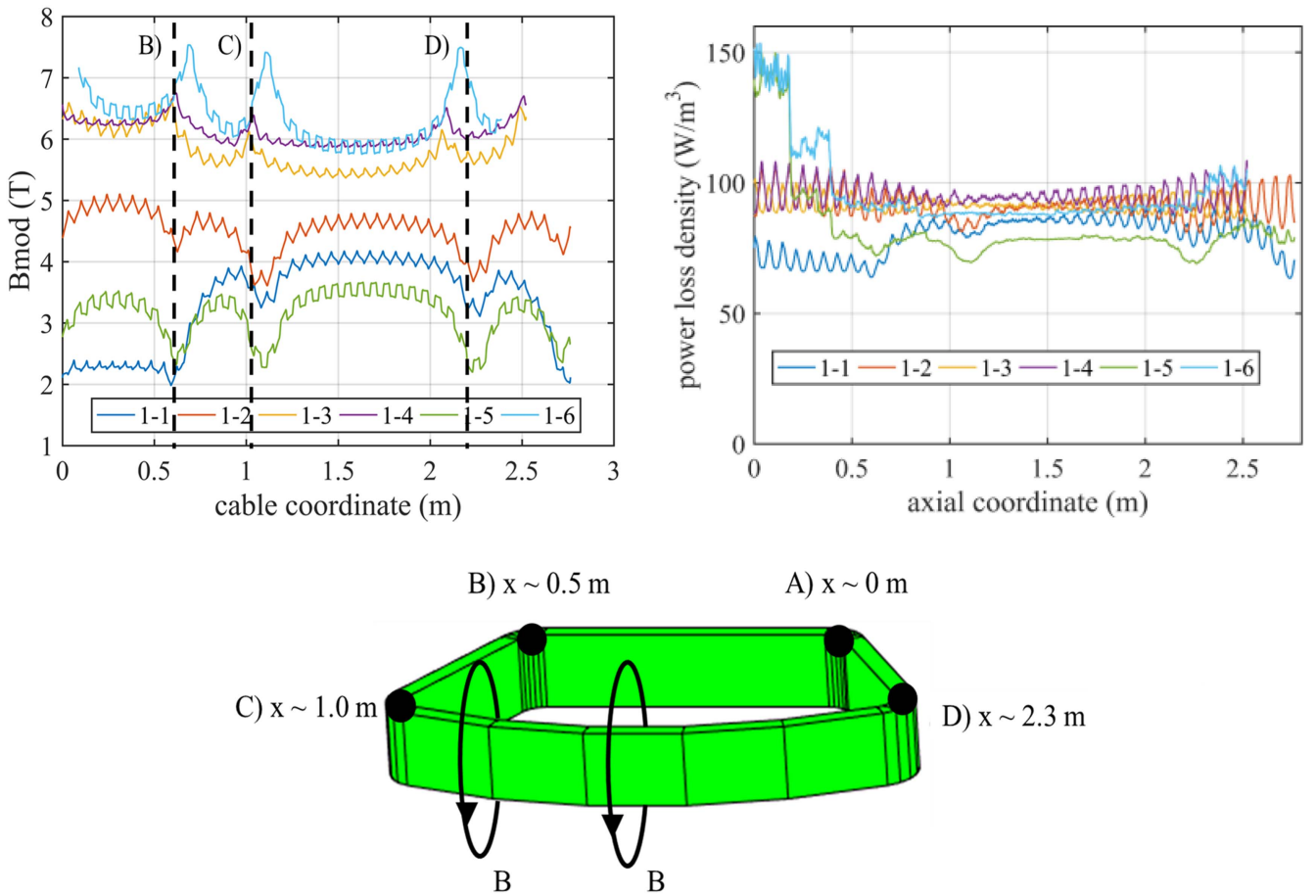

Figure 8. (a) Modulus of the magnetic flux density field on strand #1 of coil #1 at $t = 100$ s. (b) Average power loss (hysteresis + coupling) along the reference turns of coil #1 at $t = 90$ s. (c) Sketch of the different locations along the turns of coil #1.

The total power losses per unit volume along the length of turns #1 and #3 of coil #1 are shown in figure 8. The power losses closely follow the distribution of the magnetic flux density along the length of the turn. Moreover, the power losses decrease in time during the initial transport current ramp-up. As mentioned above, the hysteresis losses are dominant and depend linearly on the critical current of the wires, which decreases with increasing the magnetic flux
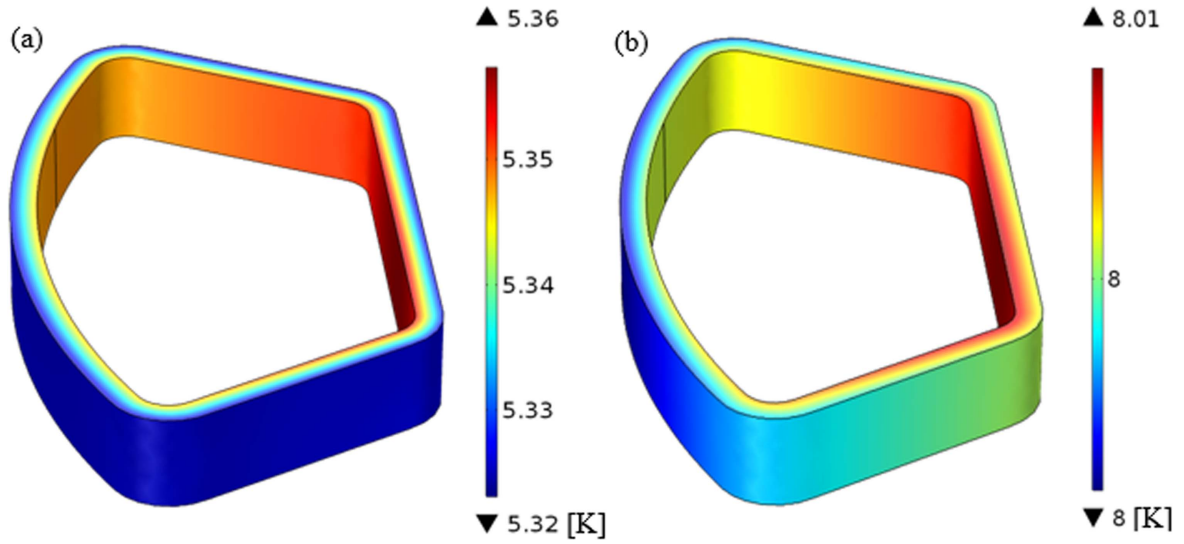
Figure 9. Temperature profile over the volume of coil #1 at (a) $t = 20$ s during the initial current ramp-up and (b) after the whole operating current cycle ($t = 440$ s).
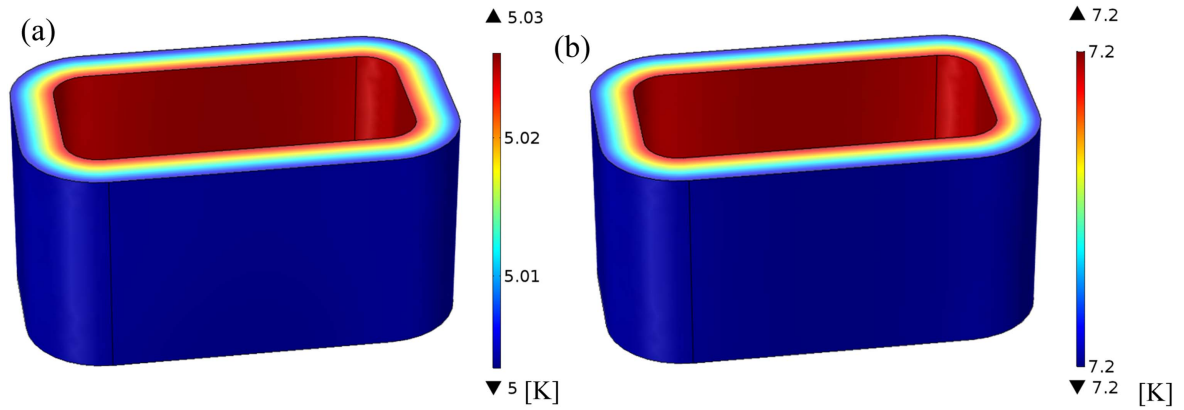

Figure 10. Temperature profile over the volume of coil #5 at (a) $t = 20$ s during the initial current ramp-up and (b) at $t = 440$ s after the whole operating current cycle.

density during the current ramp. Therefore, the initial parts of the ramp are quite delicate in terms of input power from the electrodynamic losses in these coils.

5. Thermal model of the gantry magnet system

5.1. Calculation of temperature distributions for coil #1 and coil #5

The thermal model of the magnet system solves the heat balance equation in a 3D reference system where the homogenized cable properties are considered.

$$\rho_{\text{Hom}} C_{p_{\text{Hom}}} \frac{\partial T}{\partial t} + \nabla \cdot (-\boldsymbol{k}_{\text{Hom}} \cdot \nabla T) = Q_{\text{tot}}, \qquad (6)$$

where the homogenized cable properties are considered. The parameter $\rho_{\text{Hom}} \left[\frac{\text{kg}}{\text{m}^3} \right]$ is the homogenized density, $C_{p_{\text{Hom}}} \left[\frac{\text{J}}{\text{kgK}} \right]$ is the homogenized specific heat and $\boldsymbol{k}_{\text{Hom}}$ the tensor of homogenized anisotropic thermal conductivity $\left[\frac{\text{W}}{\text{mK}} \right]$.

The materials considered in the present analysis are: copper, superconductor and bronze in the composite wire cross section, and epoxy resin in the winding pack. Their respective cross section areas are reported in table 3.

Both the specific heat and the longitudinal thermal conductivity have been homogenized accounting for the cross section areas of the coil constituting materials. The thermal conductivity in the transverse direction, instead, has been taken equal to the thermal conductivity of the epoxy resin, which represents the main thermal resistance to the flux flow in transverse direction. The validation of the homogenization procedure and the comparison with smaller volume with all the individual material components is carried on in [31]. The approach was further applied and compared with experimental results for large scale devices in [32–34].

As anticipated in the previous sections, the incoming power density from the electrodynamic losses is calculated with the THELMA code at the selected reference turns 1, 2, 3, 4, 5 and 6 of coils #1 and #5. The calculation of the

temperature rise due to these losses is performed for these two coils only, given the aforementioned symmetry conditions. Of course, the heat source obtained with THELMA has a time-dependent profile related to the magnetic flux density ramp rate. The heat source at the vertex points is interpolated in the mesh of the COMSOL model by spreadsheet tables. A further interpolation in time is required to account for the time dependence of the total losses computed by THELMA at different time instants. As mentioned above, in the para-meterization of the critical surface of the strand, the critical current depends on the magnetic flux density, and it diverges for very low values of this field. Therefore the losses diverge if the magnetic flux density gets close to zero. The influence of losses on the temperature increase is controlled by setting their maximal value to 300 W m^{-3}. The introduced maximum value is obtained for a magnetic flux density of around 0.5 T. Computations performed without limits on the AC losses maximum value show no substantial changes in the final temperature of the coils #1 and #5.

The temperature distributions of coil #1 obtained from the COMSOL computation at $t = 20$ s during the initial current ramp-up and at $t = 440$ s, almost at the end of the transport current cycle, are reported respectively in figures (a) and (b). It is worth noting that a very uniform temperature distribution is obtained both during the current ramp and at the end of the operating current cycle over the whole volume of the coil transverse cross section. This result is quite important, as it shows that the formation of hot spots is not expected in these working conditions. The same result is shown for the coil #5 in figure 9 at $t = 20$ s and $t = 440$ s. Also the coil #5 exhibits the same thermal behavior: the temperature distributions are very uniform and the formation of hot spots due to the losses in electrodynamic transients is not expected.

5.2. Computed temperature distribution versus current sharing temperature

In order to compare the increase of the coils temperature during their operating current cycle with the allowable temperature limits of the magnet, the current sharing temp-erature (T_{cs}) of the coil is computed at the peak field locations of both coil #1 and #5. Since the temperature distribution resulting from the power losses is very uniform for both coils, the temperature margin of the coil can be assessed by only considering the margin available at the location of peak field. The current sharing temperature is defined here as the temp-erature at which the electric field reaches its critical value conventionally set to $10^{-5} \left[\frac{V}{m} \right]$. Since the current sharing temperature is a function of the applied magnetic flux density, its value varies in time during the operating current cycle.

The time evolution of the current sharing temperature (T_{cs}) at the peak magnetic flux density location of coil #1 is reported in figure 10. It is worth noting that the maximal temperature reached in coil #1, 8 K, is below the lowest limit of 9.7 K set by current sharing temperature at the peak field location. The temperature margin for this coil is therefore
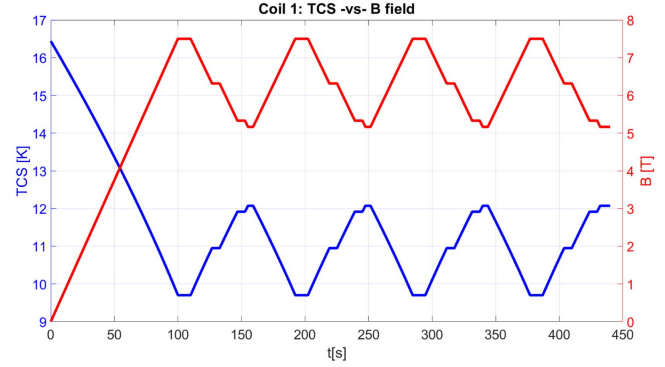

Figure 11. Profile of the current sharing temperature (T_{cs}, blue curve, primary axis on the left) and magnetic flux density at the peak field location of coil #1 (B, red curve, secondary axis).

Figure 12. Profile of the current sharing temperature (T_{cs}, blue curve, primary axis on the left) and magnetic flux density at the peak field location of coil #5 (B, red curve, secondary axis).
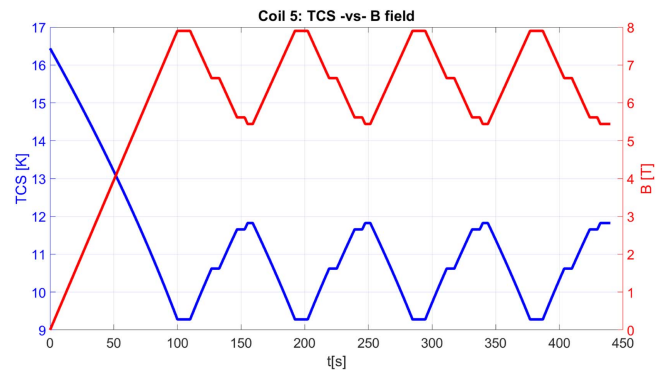
1.7 K, which is sufficient for a safe magnet design. The same considerations are deduced for the coil #5. The T_{cs} at the peak magnetic flux density location is reported in figure 11. Also in this case, the maximal temperature reached in the coil (7.2 K) is below the lowest limit of 9.3 K set by the current sharing temperature. A temperature margin of about 2.1 K is sufficient for a safe operation of the coil.

In these design considerations, it should be reminded that the temperature distribution of the coils is computed assuming adiabatic boundary conditions, which therefore give a con-servative approach.

6. Conclusion

The analysis reported in this paper is aimed at determining the losses in a superconducting Gantry magnet system for proton treatment in the frame of tumour therapy.

The THELMA model, previously developed for the analysis of the cable in conduit conductor, was adapted to analyze ac losses in the Rutherford cable configuration, and validated by comparison to analytical formulae in simplified

test cases. The code was validated for the calculation of losses in Rutherford cables by comparing analytical and numerical results in simplified cases available in the literature. The comparison shows that a good agreement can be achieved with a number of elements per cable twist pitch equal to the double of the number of strands. A variable contact conductance between strands along the cable length is essential to achieve a good agreement with the analytical calculations.

The THELMA model was then applied to the analysis of the gantry magnet system, by determining both hysteresis and coupling losses. The hysteresis losses are mainly influenced by the variation of the total magnetic field, by the critical current density and by the effective diameter of the superconducting wires. It was found that in the considered design the hysteresis losses are predominant with respect to the coupling losses. The interstrand coupling losses were computed by selecting a number of representative turns in the winding pack cross section. The THELMA code allows one to account for the magnetic field generated by all coils in the magnet system, and by all turns except for the selected one, under the assumption that the current is uniformly distributed between strands. The analysis show that the interstrand coupling losses are affected by the selection of the boundary conditions at the ends of the representative turn. The real current distribution should be included between the two extreme conditions represented by the two boundary conditions of uniform current distribution at the cable ends and of equipotential surface at the cable ends. The total losses however, are only marginally affected by the selection of the boundary conditions of the coupling loss calculation.

Due to the influence of the magnetic field on the hysteresis losses, the total losses depend on the distribution of the magnetic flux density along the length of the representative turn. On one hand, the hysteresis losses increase with the critical current of the wire, which decreases with increasing the magnetic field. On the other hand, the hysteresis losses depend on the time derivative of the magnetic flux density, which is greater at the high field locations. Although the locations of peak field generally exhibit higher losses than the rest of the winding pack, there is some compensation effect, so that the loss distribution versus location is smoother than the field distribution. As far as the time distribution of the losses, during the initial ramp of the transport current cycle, when the critical current density is high due to the low values of magnetic field, a significant input power enters the magnet system due to the electrodynamic losses.

The computed losses were implemented in an adiabatic thermal model to perform a conservative estimation on the thermal stability of the magnet system design during the operation current cycle. The computed temperature profile was compared with the time-dependent current sharing temperature, obtaining as a result a sufficiently large temperature margin, which guarantees a safe magnet design.

ORCID iDs

M Breschi https://orcid.org/0000-0001-9025-2487
L Cavallucci https://orcid.org/0000-0002-0096-4817

References

[1] Calzolaio C, Sanfilippo S, Calvi M, Gerbershagen A, Negrazus M, Schippers M and Seidel M 2000 Preliminary magnetic design of a superconducting dipole for future compact scanning gantries for proton therapy *Cryogenics* **40** 445–57

[2] Sanfilippo S, Calzolaio C, Anghel A, Gerbershagen A and Schippers J M 2016 Conceptual design of superconducting combined function magnets for the next generation of beam cancer therapy gantry *Proc. RuPAC (St. Petersburg, Russia)*

[3] Amemiya N, Sogabe1 Y, Sakashita1 M, Iwata Y, Noda K, Ogitsu T, Ishii Y and Kurusu T 2016 Magnetisation and field quality of a cosine-theta dipole magnet wound with coated conductors for rotating gantry for hadron cancer therapy *Supercond. Sci. Technol.* **29** 024006

[4] Muehle C, Langenbeck B, Kalimov A, Klos F, Moritz G and Schlitt B 2004 Magnets for the heavy-ion cancer therapy accelerator facility (HICAT) for the Clinic in Heidelberg *IEEE Trans. Appl. Supercond.* **14** 461–4

[5] Pedroni E *et al* 2004 The PSI gantry 2: a second generation proton scanning gantry *Z. Med. Phys.* **14** 25–34

[6] Gerbershagen A, Meer D, Schippers J M and Seidel M 2016 A novel beam optics concept in a particle therapy gantry utilizing the advantages of superconducting magnets *Z. Med. Phys.* **26** 224–37

[7] Noda K *et al* 2008 New treatment facility for heavy-ion cancer therapy at HIMAC *Nucl. Instrum. Methods Phys. Res.* B **266** 2182–5

[8] Iwata Y, Noda K, Shirai T, Murakami T and Furukawa T 2012 Design of a superconducting rotating gantry for heavy-ion therapy *Phys. Rev. Spec. Top., Accel. Beams* **15** 044701

[9] Iwata Y, Noda K, Shirai T, Furukawa T and Murakami T 2014 Development of curved combined-function superconducting magnets for a heavy ion rotating-gantry *IEEE Trans. Appl. Supercond.* **23** 4400505

[10] Derenchuk V 2014 'The ProNova SC360 Gantry,' *Modern Hadron Therapy Gantry Developments, Technical Report* Cockcroft Inst., Daresbury, UK

[11] Iwata Y *et al* 2016 Beam commissioning of a superconducting rotating-gantry for carbon-ion radiotherapy *Nucl. Instrum. Methods Phys. Res.* A **834** 71–80

[12] Iwata Y *et al* 2013 Development of a superconducting rotating-gantry for heavy-ion therapy *Nucl. Instrum. Methods Phys. Res.* B **317** 793–7

[13] Priano C, Fabbricatore P, Farinon S, Musenich R, Perrella M and Squarcia S 2002 A superconducting magnet for a beam delivery system for carbon ion cancer therapy *IEEE Trans. Appl. Supercond.* **12** 988–92

[14] Brouwer L, Caspi S, Hafalia R, Hodgkinson A, Prestemon S, Robin D and Wan W 2017 Design of an achromatic superconducting magnet for a proton therapy gantry *IEEE Trans. Appl. Supercond.* **27** 4400106

[15] Takayama S *et al* 2016 Thermal stability of conduction-cooled HTS magnets for rotating gantry *IEEE Trans. Appl. Supercond.* **26** 4402404

[16] Takayama S, Koyanagi K, Yamaguchi A, Tasaki K, Kurusu T, Ishii Y, Amemiya N, Ogitsu T and Noda K 2015 Design of conduction-cooled HTS coils for a rotating gantry *Phys. Proc.* **67** 879–84

[17] Breschi M and Ribani P L 2008 Electromagnetic modeling of the jacket in cable-in-conduit conductors *IEEE Trans. Appl. Supercond.* **18** 18–28

[18] Breschi M, Bianchi M, Bonifetto R, Carli S, Devred A, Martovetsky N, Ribani P L, Savoldi L, Takaaki I and Zanino R 2017 Analysis of AC losses in the ITER central solenoid insert coil *IEEE Trans. Appl. Supercond.* **27** 4200605

[19] Akhmetov A, Bottura L, Breschi M and Ribani P L 2000 A theoretical investigation on current imbalance in flat two-layer superconducting cables *Cryogenics* **40** 627–35

[20] Akhmetov A, Bottura L and Breschi M 2001 A continuum model for current distribution in rutherford cables *IEEE Trans. Appl. Supercond.* **11** 2138–41

[21] Bottura L, Breschi M and Fabbri M 2002 Analytical solution for the current distribution in multistrand superconducting cables *J. Appl. Phys.* **92** 7571–80

[22] Bottura L, Breschi M and Fabbri M 2003 Analytical calculation of current distribution in multistrand superconducting cables *IEEE Trans. Appl. Supercond.* **13** 1710–13

[23] Bottura L, Breschi M and Fabbri M 2003 An analytical benchmark for the calculation of current distribution in superconducting cables *Cryogenics* **43** 241–8

[24] *COMSOL Multiphysics User's Guide*, COMSOL, Burlington, MA, USA, 2012

[25] Schmuser P 1987 Course on acelerator optics *Proc. 986 CERN Accelerator School* pp 87–10 CERN

[26] Bottura L and Bordini B 2009 $J_c(B, T, \varepsilon)$ parametrization for the ITER Nb_3Sn production *IEEE Trans. Appl. Supercond.* **9** 1521–4

[27] Verweij A P 2006 CUDI: a model for calculation of electrodynamic and thermal behaviour of superconducting Rutherford cables *Cryogenics* **46** 619–26

[28] Wilson M N 1983 *Superconducting Magnets* (Oxford: Oxford University Press)

[29] Sytnikov V E, Svalov G C, Akopov S G and Peshkov I B 1989 Coupling losses in superconducting transposed conductors located in changing magnetic fields *Cryogenics* **29** 926–30

[30] Akhmetov A A 2000 Compatibility of two basic models describing the a.c. loss and eddy currents in flat superconducting cables *Cryogenics* **40** 445–57

[31] Casali M, Breschi M and Ribani P L 2015 Two-dimensional anisotropic model of YBCO coated conductors *IEEE Trans. Appl. Supercond.* **25** 6600112

[32] Breschi M, Cavallucci L, Ribani P L, Gavrilin A V and Weijers H W 2016 Analysis of quench in the NHMFL REBCO prototype coils for the 32T magnet project *Supercond. Sci. Technol.* **29** 055002

[33] Breschi M, Cavallucci L, Ribani P L, Gavrilin A V and Weijers H W 2017 Modeling of quench in the coupled HTS insert/LTS outsert magnet system of the NHMFL *IEEE Trans. Appl. Supercond.* **27** 4301013

[34] Morandi A *et al* 2013 Quench behavior of MgB_2 pancake coil for FCL applications *IEEE Trans. Appl. Supercond.* **23** 5600404